JOURNAL OF SPACECRAFT AND ROCKETS
Vol. 59, No. 5, September–October 2022

Remote Electrostatic Potential Sensing for Proximity Operations: Comparison and Fusion of Methods

Kieran Wilson,* Miles Bengtson,* and Hanspeter Schaub†
University of Colorado Boulder, Boulder, Colorado 80301

https://doi.org/10.2514/1.A35071

Recently, two methods have been developed for remote monitoring of spacecraft electrostatic potential from a co-orbiting craft, an important technology for preventing electrostatic discharge during initial contact, characterizing satellite surfaces during servicing missions, and accounting for electrostatic perturbations that affect relative motion during proximity operations. Each method is analyzed individually in the literature and each method has unique strengths and limitations. This work considers the fusion of data from both methods to generate an estimate of the electrostatic potential with higher accuracy and lower uncertainty than either method could provide independently. The methods involve observing x-ray and electron spectra emitted when energetic electrons, such as those from an electron source, strike the surface of a nearby spacecraft. The electron method provides a highly accurate estimate (≤10 V error) but is strongly sensitive to the relative geometry of the spacecraft, which limits the times during which a usable signal is received. The x-ray method produces a less accurate estimate (∼100 V error) but is less sensitive to target geometry and has greater signal availability. The methods are compared though experiments and a simulated servicing mission, and both estimation methods are fused to mitigate the limitations of each and produce a robust estimate of the surface voltage. Fusing the datasets produces significant improvements in accuracy and geometrical coverage of the voltage estimate across a wide range of conditions. These results are important for future missions, which must remotely monitor the potential on a nearby object to ensure mission success.

Nomenclature

A	=	state matrix
C	=	capacitance, F
E	=	photon or electron energy, keV
E_e	=	incident electron energy, keV
E_k	=	K_α transition energy for an element, keV
$E_{\delta\max}$	=	energy of maximum secondary electron yield
$\boldsymbol{F}$	=	force vector, N
H	=	measurement-to-state conversion matrix
I_p	=	characteristic photon yield
K	=	Kalman gain
K_c	=	Coulomb's constant, $14\pi\epsilon_0 \approx 8.99 \times 10^9$ N · m^2 · C^2
$\boldsymbol{L}$	=	torque vector, N · m
P	=	error covariance
Q	=	process noise matrix
q_i	=	charge on body i
r	=	normalized measurement residual
ϵ_0	=	vacuum permittivity, $\approx 8.854 \times 10^{-12}$, F/m
$\boldsymbol{u}$	=	control effort, m/s^2
V	=	electrostatic potential, V
X	=	state estimate
Z	=	atomic number
z	=	measurement vector
δ	=	secondary electron yield per incident electron

I. Introduction and Motivation

AS THE space industry considers increasingly complex missions with multiple spacecraft operating in close proximity, there is a growing need to be able to remotely characterize orbital objects from a nearby spacecraft. While a range of techniques exists for evaluating properties such as relative attitude and position, few options exist for determining the electrostatic potential remotely even though electrostatic charging can result in damaging arcing during contact or significantly affect rendezvous dynamics through perturbing forces and torques [1].

Ambient plasma fluxes and the photoelectric effect cause satellite surfaces to become electrically charged, up to thousands of volts in polar low Earth orbit or tens of kV in the hot, sparse plasma environment at geosynchronous orbit (GEO) [2,3]. Even though proximate satellites experience the same environmental conditions, they may charge to different potentials because charging depends strongly on the material properties including secondary electron yield, surface finish, and work function. Further, unique geometries experience different sunlight exposure and thus photoelectron currents, in addition to differences in plasma environments on the wake and ram sides of a spacecraft [4,5]. As a result, there is a significant risk for potentially hazardous electrostatic discharge (ESD) during initial contact between two bodies. Additionally, the charged craft create electrostatic forces and torques that affect the relative motion [1]. Therefore, it is imperative that future multispacecraft missions have a means for remotely characterizing the electrostatic state of another object.

Robotic servicing and salvaging missions propose operations in which a satellite approaches and then interfaces with a retired satellite, such as Northrop Grumman's Mission Extension Vehicle, which is designed to take over station keeping and attitude control for an out-of-fuel GEO communications satellite, or NASA's Restore-L mission to refuel Landsat-7 [6–8]. These missions require satellites to operate in very close proximity and eventually make contact with a client that is not designed to facilitate rendezvous and proximity operations. Many of these servicing concepts are focused on GEO because of the high value of operating GEO assets and low ΔV costs associated with moving between locations in GEO; however, spacecraft in these orbital regimes experience large electrostatic potentials as a result of local plasma conditions. NASA's planned Lunar Gateway program involves spacecraft docking in the outer radiation belt to transfer modules to lunar orbit. Reference [9] shows that the expected potential difference between the Lunar Gateway and Orion module prior to making contact is on the order of kilovolts. In Ref. [10], a trade space is defined of eight mission architectures for on-orbit servicers and assemblers. Any scenario involving two or more objects in close proximity without a direct conductive path

Received 19 January 2021; revision received 22 February 2022; accepted for publication 6 March 2022; published online 20 April 2022.

*Graduate Research Assistant, Ann and H.J. Smead Aerospace Engineering Sciences Department. Member AIAA.

†Glenn L. Murphy Endowed Chair, Ann and H.J. Smead Aerospace Engineering Sciences Department. Fellow AIAA.

between them would benefit from electrostatic sensing, which applies to six of the eight defined architectures for on-orbit assemblers and servicers.

Additionally, the valuable GEO region is becoming increasingly congested, and the need for active debris remediation is well-established [2]. The electrostatic tractor (ET) is an elegant solution proposed for remediation of debris from valuable orbital slots in GEO, leveraging the electrostatic forces and torques between multiple craft to control relative dynamics without requiring physical contact [11]. The ET approaches the debris object and directs an electron beam toward it to transfer charge. Subsequently, the tractor charges positively and the debris object charges negatively, which produces a resultant attractive force. The tractor then uses inertial thrusters to tug the debris object to a graveyard orbit while maintaining an offset on the order of 10 meters from the debris object [12]. Similarly, electrostatic torques can be used to detumble large objects prior to approach for servicing. This is critical because defunct GEO spacecraft and debris objects can have rotational rates of up to tens of degrees per second [13–15], which prohibits attempts to physically interface with them for servicing or reorbiting. Electrostatic force and torque solutions exist for these challenges, but control of another object requires knowledge of the forces and torques, which in turn depend on the voltages and capacitances. The capacitance of a spacecraft body is typically a function of the geometry alone, so if potentials and the spacecraft geometries are known, then the intercraft forces and torques can be evaluated using a method like the multisphere model (MSM) [16]. Given knowledge of a target geometry, only the electrostatic potential of the target craft must be evaluated to solve for the system dynamics. Remote electrostatic characterization is therefore an enabling technology for a wide range of on-orbit servicing, salvaging, and rendezvous applications.

Two promising methods for remote electrostatic characterization are examined in this paper, as shown in Fig. 1. The first method involves using the servicing craft to measure the energy distribution of secondary electrons and photoelectrons emitted by the object of interest. Both types of electrons are emitted with initial energies of a few electron volts, so the energy with which the electrons arrive at the servicing craft is equal to the potential difference through which they have been accelerated (plus their very small initial energy). Given the potential of the servicing craft, the potential of the target object is then inferred [17,18]. The second method involves measuring x rays emitted from the target surface when irradiated by energetic electrons. The maximum energy x-ray photon is equal to the landing energy of the incident electron. Thus, if the electron energy leaving the servicer is known and an x-ray spectra is collected, the target potential can be determined [19,20].

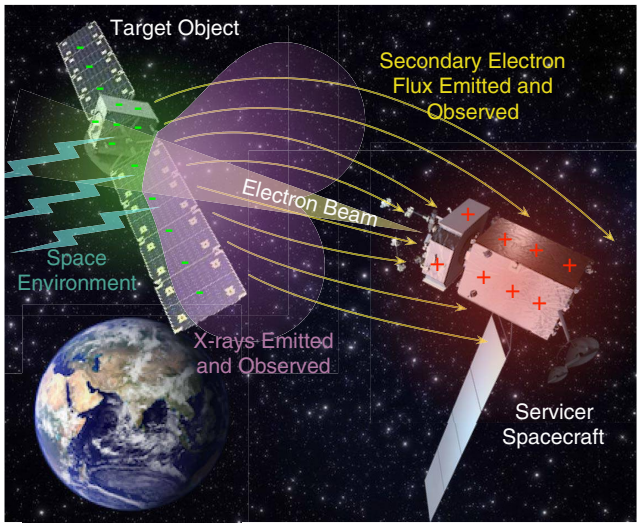

Fig. 1 Concept of operations for touchless potential sensing, using x rays and secondary electrons emitted from an object.

Each method is analyzed individually in the literature, and each method has unique strengths and limitations. This work considers the fusion of data from both methods to generate an estimate of the electrostatic potential with higher accuracy and lower uncertainty than either method could provide independently. Rather than using only one of the methods, this paper demonstrates that future missions could incorporate both sensors into an electrostatic characterization suite for more robust sensing capabilities. Furthermore, both instruments could be incorporated without adding significant complexity or requirements to the servicing spacecraft. Both x-ray and electron analyzers have extensive flight heritage. It is emphasized that this work is not proposing new hardware, but rather using existing hardware in a novel way to obtain useful information in the context of orbital robotics missions. By using both types of sensors in a collaborative implementation, a target can be electrostatically characterized better than is possible with just one type of sensor.

This paper focuses on two methods for determining the electrostatic potential on a body remotely, comparing the methods through analysis of both the electron-based method and the x-ray spectroscopic method, experiments, and simulation of a servicing mission. A method for improving estimates of a target's electrostatic potential by fusing both methods is presented in Sec. IV.

II. Review of Remote Potential Determination Methods

A. Electron Spectroscopic Method

When an energetic electron impacts a surface, it produces additional electrons that are emitted from the surface at energies of a few electron volts, known as secondary electrons. The peak of the secondary electron initial energy distribution is equal to one-third the work function of the surface material, which is typically a few electron volts [21]. The number of secondary electrons produced for a single incident electron is known as the secondary electron emission (SEE) yield, a material-dependent property that is a function of the incident electron energy and angle. For many materials, there is a range of incident energies for which the SEE yield exceeds unity, indicating that a single incident electron causes multiple electrons to be emitted. The SEE yield typically increases as the incident beam becomes more off-normal to the surface [22]. This is because, for shallow angles, the incident particles deposit more energy closer to the surface, generating secondary electrons with a greater chance of escaping the material.

The prospects and challenges of the electron method for remote potential sensing are discussed in Ref. [17] but are briefly reviewed here. The electron method for remote sensing leverages the fact that secondaries are generated with very small initial energies to achieve high resolution, regardless of the incident particle energy. A servicing craft approaches the object of interest and achieves a positive voltage relative to it by emission of an electron beam. Depending on the application, the electron beam may be directed toward the object to transfer charge (for electrostatic actuation, for example) or off into space. Secondary electrons are generated on the surface of the target object either by the active electron beam or by ambient plasma currents in GEO. They are then accelerated by the electric field toward the servicing spacecraft where they are observed with an electron energy analyzer. Electron energy analyzers are ubiquitous on satellites and therefore have extensive flight heritage (e.g. [23–26]). The energy of the electrons is equal to the potential difference between the two craft, as they are assumed to have a negligible energy of a few electron volts when emitted. Therefore, if the voltage of the servicing craft is known, the voltage of the object of interest can be determined.

There are some limitations, however. First, a sufficient number of electrons must be generated such that the energy analyzer can detect the signal in the ambient plasma background. Reference [17] demonstrates that, for several different representative flight scenarios, the signal generated from a target spacecraft is sufficiently large to be measured relative to the background plasma, especially because the signal consists of electrons with discrete energies, whereas the background contains a spectrum of energies. Second, the electron trajectories are determined by the electric field between the two craft. The

electric field is a product of the target's geometry, as is discussed in Sec. V. Therefore, the electrons generated on the target may not fly toward the sensing craft unless the sensing craft is in a favorable relative position. Objects in GEO are commonly tumbling, so there will be times and relative attitudes for which the target voltage is unobservable using the electron method. This effect can be mitigated in part by defocusing the incident electron beam to illuminate the entire visible side of the target, maximizing the likelihood of a detectable signal.

An example secondary electron spectrum collected by a retarding potential analyzer (RPA) is shown in Fig. 2. To obtain this data, an electron beam is directed at an aluminum plate that is held at a fixed potential of −511 V (indicated by the dashed vertical line in both panels). The RPA consists of two metallic grids in front of a collector. The front grid is grounded, and a discriminating voltage is applied to the second grid to exclude electrons with energies less than the discriminating grid voltage. The top panel of Fig. 2 shows the current-voltage curve. Taking a derivative of this gives the actual electron energy distribution, as shown in the lower panel. A Gaussian curve is fit to the electron energy distribution data, and the peak of the curve is taken as the estimate of the plate potential. For the example shown, the estimated voltage is −518 V whereas the actual plate voltage was −511 V. This gives an error of 1.37%. The 95% confidence bounds on the Gaussian fit are taken as the uncertainty associated with the measurement. The noise floor of the electron energy distribution is 0.0605 nA/eV, whereas the peak of the Gaussian model is 1.308 nA/eV, giving a signal-to-noise ratio (SNR) of 21.6. As the total signal received by the RPA decreases, the peak height of the energy distribution tends toward the noise floor, and the uncertainty bounds increase toward infinity. Therefore, the measurement can be effectively weighted in a filtering algorithm by the height of the peak compared to the noise floor.

Several systematic errors contribute to the accuracy of the electron method. First, the RPA is ultimately a velocity filter, not an energy filter. Though it excludes particles with energies less than the discriminating voltage, it can also exclude particles with higher energies if those particles are not moving along the axis of the instrument (i.e., normal to the grids). Off-axis particles are rejected when the voltage on the grid is lower than their total energy. Thus, any misalignments in the system cause the electron energy distribution to appear to shift to lower energies. The shift in energy is given by the following equation [27]:

$$\frac{\Delta E}{E} = \sin^2\theta \tag{1}$$

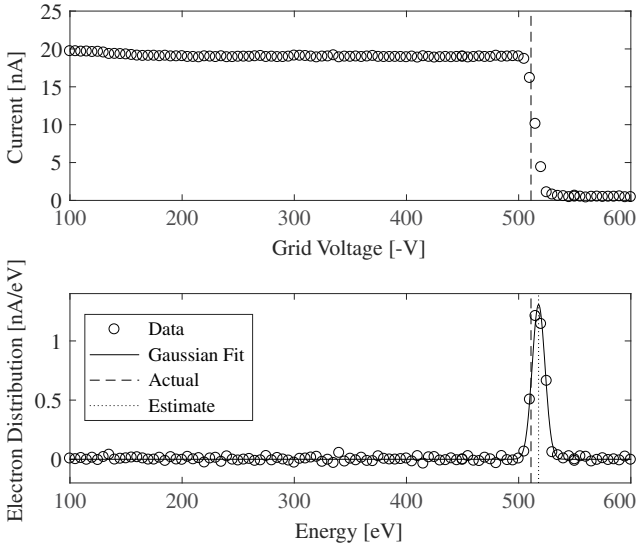

Fig. 2 Example electron spectrum generated by a 10 keV, 10 μA electron beam incident on an aluminum plate.

where θ is the off-axis angle of the particles. Even though the aperture of the RPA is pointed directly at the electron beam spot on the plate, the electric field from the plate and ambient magnetic field can steer the particles such that they enter the RPA at an angle. The ambient magnetic field in the vacuum chamber is on the order of 40 μT. For a 500 eV electron, this gives a gyroradius on the order of 1.9 m whereas the diameter of the chamber is only 0.56 m and the separation distance between the plate and the instrument aperture is only 0.25 m. Another factor is caused by the finite dimensions of the RPA grids, which create imperfect equipotential planes because the voltage in the center of a grid square is less than the voltage applied to the actual grid wires [27]. This causes a broadening of the electron peak, which, for the RPA used in the experiments, results in an increase of the peak width of $(\Delta E/E) = 2.1\%$. Finally, the secondary electrons are generated with a small initial energy distribution that also contributes to the peak location and width. Finally, contaminants and oxide layers on the target surface cause small, localized potential variations on the order of a volt, which affect the measured plate potential [28].

Though in this case the estimate is slightly larger (in magnitude) than the actual plate voltage, this is not always the case. The measurement is affected by the alignment of the RPA relative to the particle flight directions, the design of the RPA, and the surface conditions of the target. Recent experimental campaigns have shown that the electron method is accurate to within a few percent error for a wide range of test conditions and there is not a systematic bias to estimate higher or lower [18].

B. x-Ray Method

1. *Active Sensing*

As electrons interact with electric fields around atomic nuclei, they undergo accelerations. Each loss of kinetic energy is emitted as a photon in a continuous spectrum, through a process known as bremsstrahlung. The upper limit of the energy that can be radiated in a single interaction is equal to the initial kinetic energy of the electrons, which provides a means to determine the landing energy of the electrons [29]. The electrons can take an infinite number of trajectories in the vicinity of the nucleus, such that every photon energy up to the landing energy of the electrons is emitted. A continuous x-ray spectrum is formed, as each x ray observed corresponds to a specific interaction between an atom and an incident electron. If the initial energy of the electrons is known, whether from a servicing spacecraft's electron beam or the ambient plasma environment, the potential difference between a servicer and a target can then be inferred based on the change in energy of the electrons. The viability of this concept for spacecraft potential determination is theoretically explored in [19], while preliminary experiments are presented in Ref. [20]. This study finds that determining the landing energy of a beam to less than 1% error is readily achievable using commercially available detectors with prior flight heritage.

As seen in Fig. 3, the landing energy can be determined by fitting a line to the upper energy part of the sensed x-ray spectrum. The intercept between the line and the x axis is then taken to be the landing energy of the electrons, in a method proposed in Ref. [30]. This method is less sensitive to extraneous x-ray sources or noise than simply taking the highest energy photon collected to be the landing energy, resulting in a more robust estimate of landing energy.

The bremsstrahlung radiation, and particularly the highest energy part of the spectrum, is directionally dependent, which impacts the accuracy of the sensed landing energy. Likewise, there are limits to the physical sensors used to observe the x-ray spectrum. An Amptek X123 Si-PIN diode detector was used for these experiments, as this detector is highly compact, requires no external cooling, has prior flight heritage, and has a very good energy resolution of 120 eV [31]. The landing energy uncertainty is determined from a statistical assessment of the line of best fit by adding bounding lines to cover 95% of the sampled data points. The x-intercepts of these bounding

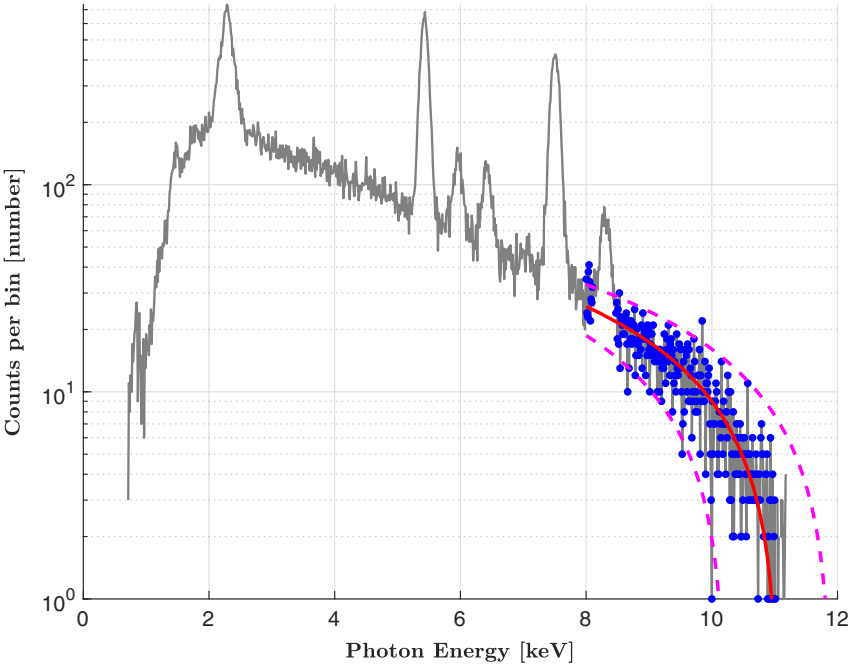

Fig. 3 Example x-ray spectrum generated by 11 keV electrons on an inconel target. The peaks are caused by characteristic elemental transitions, while the red line is fit to the blue points to determine the landing energy of the electrons.

lines are then used to establish bilateral uncertainties for the landing energy estimate.

2. *Passive Sensing*

While bremsstrahlung radiation can be generated through the use of an active electron beam on a servicer, the space environment can contribute a significant population of energetic electrons without the need for an active electron beam. Unlike the electron beam-based method, this electron population does not have a single unique energy, but is rather described by an energy spectrum. This makes deconvolution of the resultant x-ray spectrum to determine the incident electron population difficult, but an alternative method can be used to determine the relative potential of a target body.

This alternative evaluates the total number of photons observed from the target and uses variations in the photon flux to estimate changes in potential. A surface charging negative will repel low-energy electrons and reduce the energy of the remainder of the electron spectrum. Therefore, negative surface charging leads to a net decrease in both the number of electrons impacting the surface as well as their energy; this ultimately leads to a reduction in x-ray generation from both bremsstrahlung and characteristic radiation. Negative charging will accelerate ions toward the surface, increasing their impact energy, but ions have far lower bremsstrahlung and characteristic radiation yields than electrons and are likely negligible contributors to the x-ray spectrum in the range of interest.

Changes in photon emission can also result from changes in the ambient plasma, so an electron energy analyzer must be used in tandem with an x-ray detector to account for these ambient plasma changes. Additionally, this method only provides a measure of relative changes in potential on the target and does not provide an absolute measure or a measure relative to the servicer. This passive sensing method is also less accurate than other methods but does provide an independent check on the beam-based x-ray potential determination method and the electron-based method.

Two dominant components of the x-ray spectrum are assessed to determine the theoretical photon flux: the flux of bremsstrahlung and characteristic photons as a result of ambient plasma electrons, and those emitted by an incident electron beam. The spacecraft model was assumed to be entirely aluminum for this analysis, providing a conservative estimate of the bremsstrahlung yields.

The bremsstrahlung spectrum emitted by incident electrons is approximated by the empirically fit equation

$$\Delta = C\sqrt{Z}\frac{E_e - E}{E}\left(-73.90 - 1.2446E + 36.50 * \ln Z + \frac{148.5E_e^{0.1293}}{Z}\right) \times \left[1 + (-0.006624 + 0.0002906E_e)\frac{Z}{E}\right]\Delta E \tag{2}$$

provided by Ref. [32]. This equation is valid for photon and electron energies of interest, with a detector sensitive primarily to photons in the 1–30 keV range. This can be combined with an equation describing characteristic radiation to evaluate the complete x-ray spectrum.

Characteristic radiation yield from the K_α transition per incident electron is given by [33]

$$I_p = N\left(\frac{E_e}{E_k} - 1\right)^\alpha \tag{3}$$

Assuming an aluminum target, the parameters are approximately $N = 1.4 \times 10^{-5}$, $\alpha = 1.63$, energy of characteristic emission $E_k = 1.49$ keV, and incident electron energy is given by E_e [33]. Each incident electron with an energy greater than the characteristic energy can therefore result in the release of a characteristic photon, and the probability of characteristic emission increases with increasing incident electron energy.

The relations for x-ray emission as a function of electron energy in Eqs. (2) and (3) are then used to estimate the relative x-ray flux as a function of surface potential, assuming the source electron spectrum is constant. The plasma electron spectrum would be continuously monitored using the electron energy analyzer, and the theoretical photon output could be updated if a significant change in electron spectra is observed.

This passive sensing concept can be experimentally validated through the use of a broad-spectrum electron gun, capable of generating a tunable spectrum of electrons to mimic the plasma of a space environment [34]. The broad-spectrum electron gun is aimed at an aluminum target plate. The potential of the target is independently regulated by a high-voltage power supply, while the Amptex X123 x-ray spectrometer is used to observe the x-ray spectra emitted from the target.

Figure 4 illustrates the change in photon observations as a function of the plate potential, based on the electron spectrum generated by

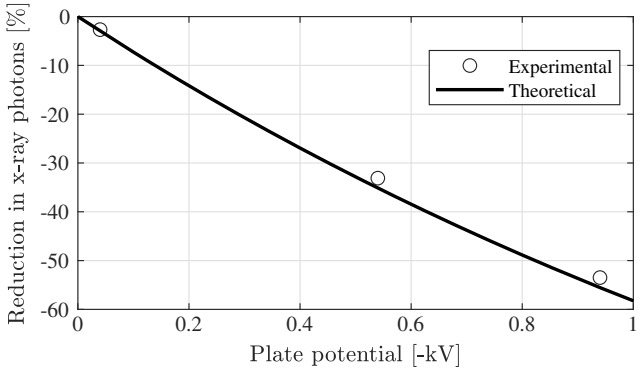

Fig. 4 Comparison of theoretical relationship between plate potential and photon emission with experimental results at three plate potentials.

setting the broad-spectrum electron gun to a maximum energy of 5 keV. As the plate potential magnitude increases, the resultant photon counts are expected to decrease according to the theoretical curve. This trend correlates well with the experimental results for this case, with errors of less than 40 volts for all points.

This method of estimating the electrostatic potential on the plate is dependent on knowledge of the electron spectrum, which can limit its applicability, and, because it is dependent on both x-ray and electron sensors, it may not always serve as an effective differential check on the estimates from other methods. However, this method does not require any active electron beam use and will not change the target's potential, and therefore it can be used to monitor the change in potential of a target due to just the space environment.

C. Experimental Validation

Previous studies [18,20,35] experimentally investigate both methods for potential estimation, though each method was considered individually. In this study, new experiments are conducted that facilitate fusion of electron and x-ray data for experimental investigation of the combined sensing technique. Specific experimental conditions that span the regions of observability for each method are selected. Data are collected in a space environment simulation chamber at the University of Colorado Boulder, which is detailed in Ref. [36]. Figure 5a shows a schematic of the experimental setup in the vacuum chamber, while Figure 5b shows a picture of the experiment as constructed. A Kimball Physics EMG-4212 electron gun is used to irradiate an aluminum target plate, generating secondary electrons and x rays. The target plate is mounted on a rotating stage controlled by a stepper motor. The plate potential is regulated by a high-voltage power supply. An Amptek X-123 x-ray spectrometer with a Si-PIN detector is used to observe the x rays. This device has prior flight heritage on the MinXSS smallsat solar observatory mission, and has a mass under 180g, including control electronics, and the actual sensor fits into a volume of 3 by 2 by 1 cm. The sensor and control electronics consume less than 2 watts total [37]. A custom-built retarding potential analyzer (RPA), approximately 15 cm in length and with a 2 cm aperture diameter, is used to measure the electron current. Flight versions have been designed to be smaller, with masses of less than 1 kg and power consumptions of less than 5 watts [38]. A Keithley 2401 pico-ammeter is used to measure the secondary electron current.

In the first experiment, both the target plate and instruments maintain fixed positions. A known voltage was applied to the plate and 60 m easurements with each method were collected, which were then used to generate synthetic datasets to demonstrate the performance of the adaptive filtering method proposed. In the second experiment, the instruments are held at a fixed location while the plate rotates through 360 deg, analogous to a target body rotating relative to a servicer. While the plate is only rotated about one axis here, similar results would be expected if the plate were rotated about the second axis instead. The results of these experiments are discussed in the following section.

III. Comparison of Touchless Potential Sensing Methods

While both x-ray and electron spectra can be collected from a single target simultaneously, there are significant differences in performance between the methods, particularly in accuracy and signal availability.

The x-ray method tends to have higher uncertainties (around 100 V, typically) in the measured potential than the secondary electron method (less than 10 V, typically), for cases with good signal-to-noise ratios for both methods. This difference is largely due to the more stochastic processes underlying bremsstrahlung generation and emission, and the increased noise sources in the x-ray sensor compared to the RPA. However, the x-ray spectra can be collected in as little as a second, while electron spectra require up to a minute using the power supplies available here. Each method therefore has unique strengths that allow them to be used in a complimentary fashion.

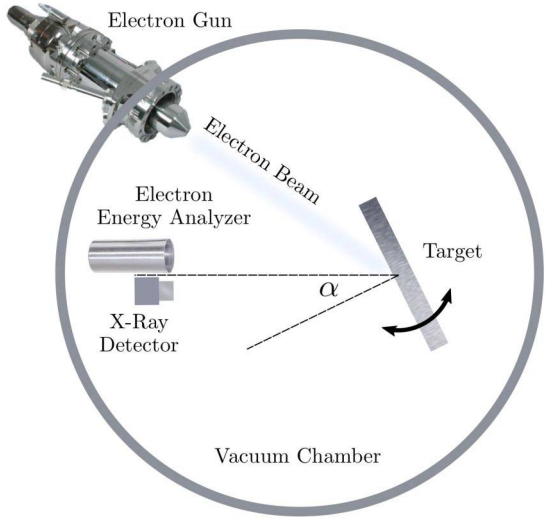

a) Schematic of the experimental setup in the vacuum chamber

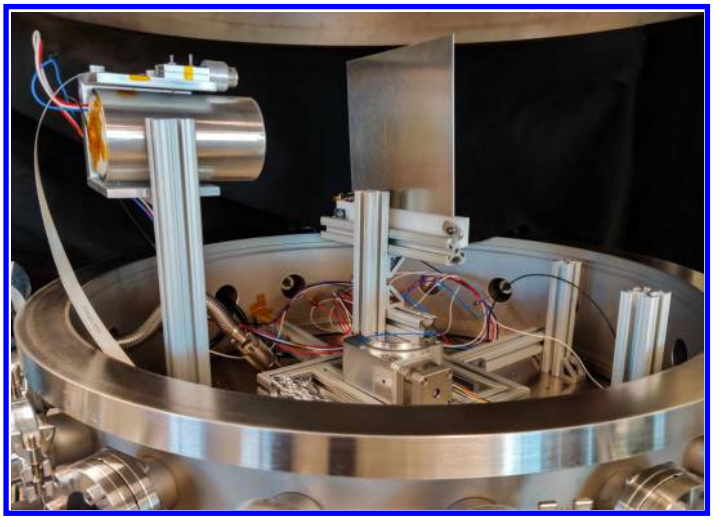

b) Picture of experimental setup inside vacuum chamber. The target plate is to the right, and the x-ray detector is mounted on top of the RPA to the left

Fig. 5 Experimental setup used to validate electron and x-ray based sensing modalities. The target plate is mounted to a rotary stage, while the detectors are held fixed.

While accuracies and sampling rates are important considerations, they are only relevant if a signal is actually observable. Both methods rely on unique physics, which impacts signal availability.

Bremsstrahlung emission has a high level of directional dependence, with the intensity and shape of the spectrum varying as a function of the angle from the incident electron beam. Prior work demonstrates that the bremsstrahlung method accuracy varies as a function of the angle between the detector and the incident beam for a given beam energy [39]. The secondary electrons likewise have an angular distribution that affects the collected yield at a given position, but this angle is relative to the local surface normal and can be dominated by electric fields resulting from target geometries. In an operational scenario, the servicer translates relative to the target, and the target is likely to be rotating relative to the servicer. However, the instruments and the electron beam would be mounted at fixed points on the servicer. This results in a constant angle between the sensors and the electron beam, so the x-ray sensor will always be observing the same portion of the bremsstrahlung spectrum. The orientation relative to the target's surface will be varying with time, so the secondary electron flux observed changes significantly.

An experiment is conducted with a rotating plate to demonstrate the effect of a nonstationary target on the signal observed by each detector, analogous to a servicing mission with a rotating target. This experiment consists of the same aluminum plate mounted to a rotational stage, while the sensors are in a fixed position inside the chamber. The potential of the plate is held at −511 V by a high-voltage power supply, and the plate potential is held constant while the plate rotates. This is analogous to a flight scenario, where the sensors are in a fixed position relative to the electron beam, but the angle relative to the target is time-varying. In this experiment, the target was held stationary while electron and x-ray spectra were collected. After collecting a spectrum at a given point, the plate was rotated by 5 deg, and a new spectrum of each type collected. The plate angle is defined as the angle between the plate normal and the instrument positions. Therefore, angles of 0 deg, 180 deg, and 360 deg indicate that the plate is facing the instruments. The electron gun parameters were held constant throughout the experiment at 10 keV emission energy and a beam current of 10 μA.

Figure 6 illustrates the uncertainty in potential estimation for both methods as a function of plate angle relative to the detector. At some angles, particularly around 0 and 180 deg, the electron-based method returns highly confident results with uncertainties of less than a volt. As the plate rotates, significant variation (over five orders of magnitude) is observed in the uncertainty in the target potential based on the electron data. In comparison, the x-ray data never has an uncertainty of less than 100 V but also has less than a 50% variation over all angles, though with zero signal availability in some regions.

Figure 7 shows the mean collected electron current as the target plate rotated through a full revolution for several plate voltages, with a constant set of electron beam parameters (10 keV, 10 μA). Note that a measurable peak in the electron data is only obtainable if the total signal is greater than 0.8 nA. During each test, the total signal

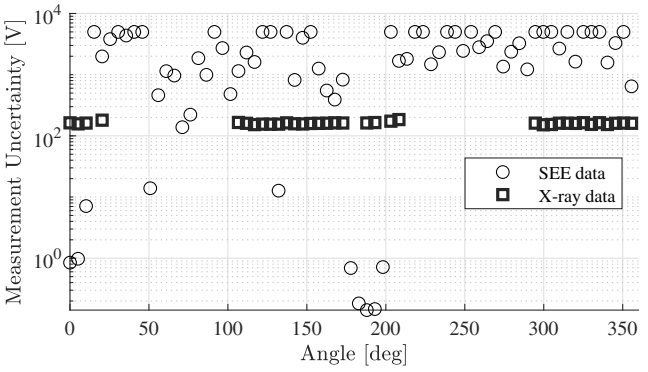

Fig. 6 Uncertainty in plate potential determination as a function of target plate angle.

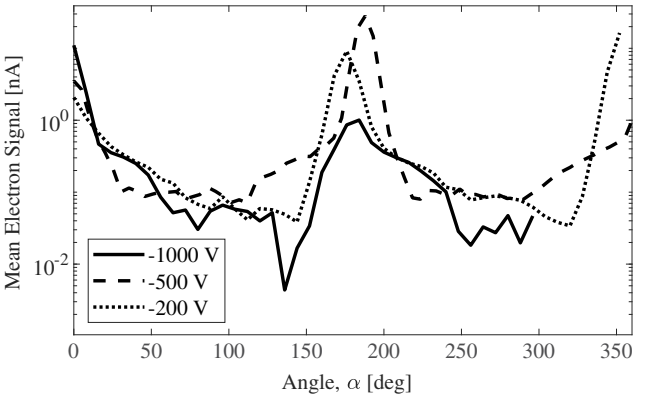

Fig. 7 Mean SEE signal as a function of angle between the plate normal and the instrument location for various voltages.

exceeded this threshold 17% of the time. Therefore, the SEE method only produces quality measurements for a narrow range of angles when the detector is located near the plate normal. The distribution of electrons from more complex target shapes is explored through simulation in Sec. V.

For the x-ray method, some target plate angles reveal additional characteristic x-ray peaks in addition to those expected from the aluminum target. The presence of these peaks can be used to identify the elemental composition of a target surface, which may be useful in mapping materials across a spacecraft surface or determining the source of anomalous results in a vacuum chamber. These peaks were found to correspond to iron and chromium, indicating that the electron beam was impacting not only the target, but the chamber walls as well. While the plate was held at a fixed nonzero potential, the chamber walls were grounded, so the bremsstrahlung spectrum would be a combination of contributions of electrons with two different landing energies. Therefore, runs with characteristic peaks of iron and other elements not found in the 6061 aluminum target plate were discarded. Future work aims to resolve multiple electron landing energies in a single bremsstrahlung spectrum, but the method applied here is valid for only one. Ultimately, the electron beam was impacting only the aluminum target for 56% of the plate's rotation. Another 21% of the positions yielded a mix of signals from the chamber walls and the target plate and had to be discarded in this analysis, while the remaining 23% were very low signal yields that made material identification and landing energy determination unreliable. The regions of each type of signal are shown in Fig. 8. In a space scenario, the portion of the electron beam that does not hit the target will instead continue off into space, resulting in a reduced, but uncontaminated, x-ray spectrum from the target. The regions in this test where both aluminum and steel signatures were observed are highlighted in Fig. 8.

It is possible to obtain a signal from at least one of the methods through almost all angles, even with the x-ray measurements being limited due to the electron beam impinging on the chamber walls. Without these contaminating cases, a usable x-ray spectrum would be observed in over 75% of cases, with fairly consistent uncertainties and errors (as seen in Fig. 6). Periods of unobservability were due to the angular separation between the electron beam and the detector, where the electron beam would impact the face of the target plate opposite from the x-ray detector. Co-alignment of the electron beam and x-ray spectrometer aperture would eliminate these periods of unobservability, though electron beam deflection could limit the generated x-ray flux [40].

While the SEE data provide a highly accurate solution with low uncertainties when the geometry is optimally oriented, the confidence in the computed solution quickly decreases for off-normal geometries because no electron signal is actually measured. The uncertainty from the x-ray method is large in the best cases but varies far less as the target rotates. The relationship between angle and uncertainty for the stationary plate case is illustrated in Fig. 6.

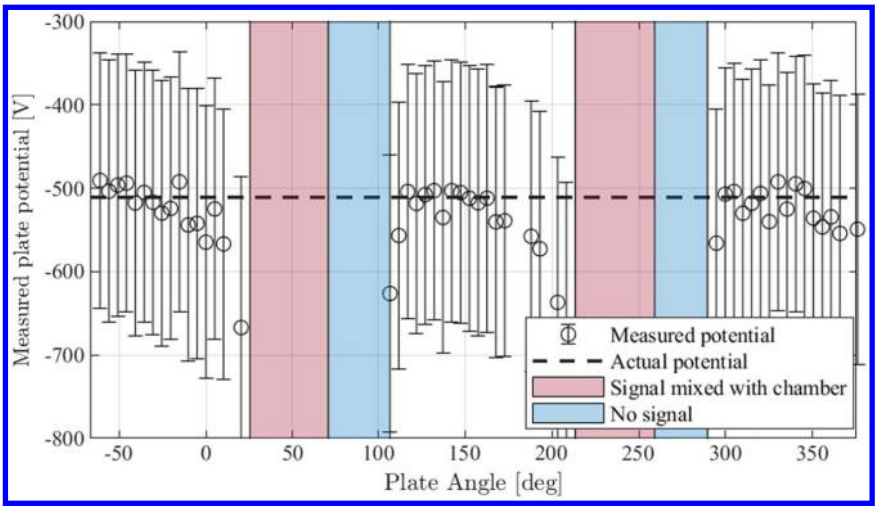

Fig. 8 Estimated plate potential as a function of angle using x-ray method, showing regions with usable signal availability.

IV. Fusion of Potential Sensing Methods

A. Adaptive Filtering

Each method has unique strengths and limitations, which makes fusing the data from each sensor appealing. Data fusion is often performed through the use of a Kalman filter, which requires some underlying dynamical model of the system, in this case, the evolution of the target body potential.

On-orbit charging involves a range of current sources, dominated by interactions with plasma electrons, ions, photoelectrons and the backscattered and secondary electrons associated with those currents. For a given space environment condition, spacecraft reach an equilibrium potential very quickly (typically seconds or less) [41]. All of these currents are highly dependent on material properties and the spacecraft surface potential, which makes developing an accurate dynamic model of the charging very challenging. The charge state evolves on the order of minutes to hours as space weather conditions change. However, after reaching an equilibrium potential, spacecraft tend to vary in potential quite slowly, such that a steady state approximation could be applied in filter development in the absence of a higher-fidelity model.

An alternative model-free method that better captures changing potential measurements is a filter that adapts the process noise parameter as a function of the uncertainty normalized residual at each timestep [42]. The filter estimates the potential at a given timestep, and then computes the residual of the actual measurement at that timestep. This residual is then normalized by the uncertainty in the measurement, which prevents particularly noisy results (such as SEE data with a very low SNR and resultant very high uncertainty) from triggering a dramatic change in the process noise. The normalized residual is then checked and, if it exceeds a tunable threshold (0.4 was used here, based on observations of the actual noise of the measurements and expected changes), is used to scale the process noise. Therefore, if a measurement with a high residual but low uncertainty is observed, the filter will significantly increase the process noise to account for the (presumed) change in target state. This method was found to be more effective at tracking transients, such as those that could be expected during an eclipse crossing, than alternative methods such as adding a fading memory term to the steady state filter.

Algorithm 1: Adaptive Kalman filter pseudocode implementation [42]

1 $1Xp_i = AX_{i-1}$ Prediction of the estimate;
2 $r_i = \dfrac{z - Xp_i}{R}$ Compute normalized residual;
3 **if** $r_i > 0.4$ **then**
4 $Q = Q(1 + r_i)$ If normalized residual exceeds threshold, scale process noise;
5 **else**
6 $Q = 1$
7 **end**
8 $Pp_i = AP_{i-1}A^T + Q$ Prediction of error covariance;
9 $K_i = Pp_iH^T(HPp_iH^T + R)^{-1}$ compute Kalman gain;
10 $X_i = Xp_i + K_i(z_i - HXp_i)$ compute state estimate;
11 $P_i = Pp_i - K_iHPp_i$ compute error covariance

For the steady-state assumption, the Kalman filter system state matrix A is set equal to identity. The states and the system state matrix are both scalars since only the target potential is to be estimated. The measurement vector z consists of the x-ray measurement and electron measurement for a given timestep stacked into a 2×1 vector. The measurements are directly equal to the state of interest, so the measurement-to-state conversion matrix H is a 2×1 vector of ones. The process noise matrix Q (in this case a scalar quantity) is tuned, and good filter performance with satisfactory convergence (to within 10 V of a truth value after initialization at a 500 V error in under 10 iterations) occurs when Q is set to identity.

To generate a dataset for filtering use, an experiment is conducted with an aluminum plate maintained at a fixed potential (−900 V). The electron gun then targets the plate with a fixed energy and current 10 keV and 10 μA, while electron and x-ray spectra are collected. A total of 60 spectra of each type are collected. These spectra are used to generate a set of measurements that are superimposed on a desired trend to simulate an eclipse scenario, as seen in Fig. 9. This provides a dataset to compare performance of the steady-state and adaptive Kalman filters. The adaptive filter performed much better over the dataset shown in Fig. 9, with mean errors of less than 50 V, less than one-third of the errors from a filter without adaptive process noise terms.

Ultimately, this process provides an example method for fusing data from both sensors and accounts for the uncertainty in the potential estimated by each sensing method at each time step. As discussed previously, depending on the relative geometry between the target and the servicer, only a degraded or insignificant signal may be available for each method. Therefore, this filter could effectively combine the measurements to attain an estimate with the overall signal availability of the x-ray method and the accuracy of the electron-based method when a signal is available.

B. Three-Way Change Detection

The three sensing methods here provide two independent measures of a target's potential (x-ray spectroscopy and electron spectroscopy) and one method that is dependent on the other two (x-ray flux intensity). This can prove a challenging scenario for error resolution, as an erroneous reading from one sensor will result in errors in two of the three potential estimates. However, some errors

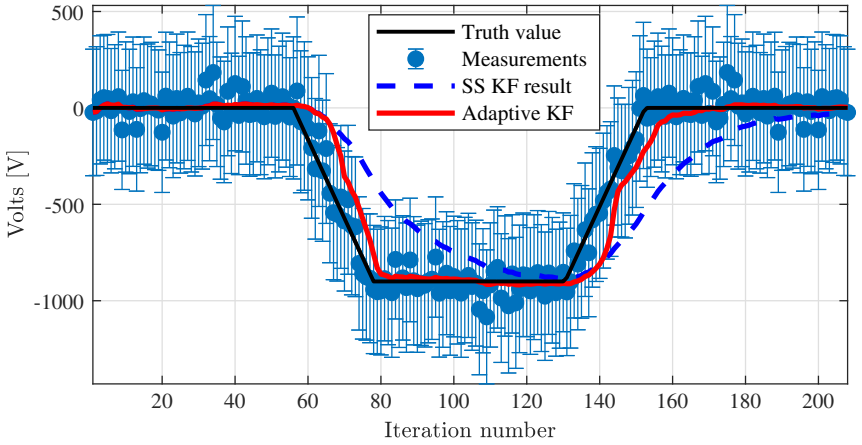

Fig. 9 Application of adaptive filter to simulated data with eclipse-like transients.

can be isolated to a single measurement. For instance, errors in the electron gun emission energy would result in incorrect determination of the relative potential using the active x-ray method, but this would not result in a corresponding change in electron spectra or passive x-ray fluxes from the target. Therefore, fault detection, isolation and recovery may be improved through the use of this combination of sensing methods, improving the likelihood of mission success.

V. Simulation of Spacecraft-Servicing Scenario

A numerical simulation of a spacecraft rendezvous scenario provides an example of how these systems could be used in practice with more complicated target geometry than a flat plate. A target with an uncontrolled 0.2 deg/s tumble rate is established, and the returned electron and x-ray photon fluxes are computed as the servicer approaches from 100 to 10 m. The target body model, which consists of a rectangular bus with a single solar array, is shown in Fig. 10.

A. Electron Signal Analysis

A simulation is developed to model the fluxes of electrons around the target to determine the expected electron signal as the servicer craft approaches the target. To gain insight into the electron distribution, only electrons generated in-plane with the servicer (along the $Z = 0$ m plane in Fig. 10) are considered, though this methodology can be extended to a three-dimensional simulation as necessary.

First, the target geometry is discretized into triangular elements (as seen in Fig. 10), and the target capacitance matrix is computed using the method of moments [43,44]. The target is assumed to be continuously conducting and therefore equipotential, allowing the charge on each triangular element to be determined. Next, the method of moments is used to determine the electric field at a given point by numerically integrating over the charge of each triangular element.

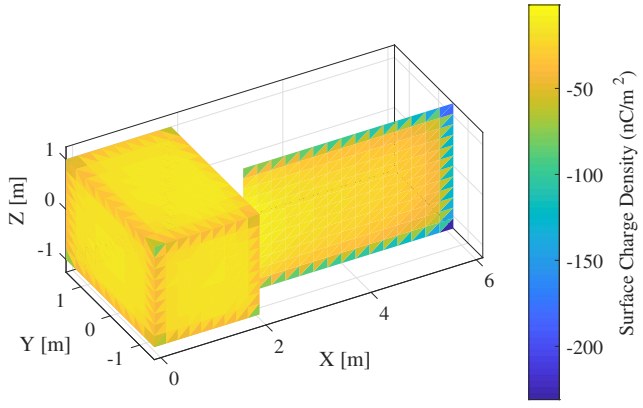

Fig. 10 Target spacecraft body.

Given the electric field, the motion of an electron near the target can be integrated using the Boris algorithm [45,46]. Figure 11 shows electrons being emitted from the target surfaces. The geometry of the target focuses or deflects the emitted electrons. Note the plot is not symmetric about the x axis because the solar panel on the right side of the box is located at $y = -0.5$ m rather than at $y = 0$ m. Particles are generated on the target centerline with a constant linear density of 60 particles/m. As a result, the relative density of the particle trajectories (black lines) corresponds to signal magnitude. For example, the electric field near the corners of the box or end of the solar panel spreads particles out, resulting in a lower signal. Particles near the interior corner where the solar panel meets the box are focused into a smaller spatial region with a large signal. A total of 1080 particles are simulated in the x–y plane, with each generated evenly on the target surface with zero initial velocity. Though the presence of a magnetic field affects the particle trajectories through gyromotion, the gyroradius for 5 keV electrons interacting with the relatively low magnetic fields at GEO is over 2 km; even 500 eV electrons have gyroradii of 800 m, much larger than the distances of interest here (<100 m). Therefore, the magnetic field is assumed to be zero here to allow the effects of the target geometry to be investigated with greater clarity.

Figure 12 shows the location of the servicing craft in the target body frame (red dots), along with the electrons emitted from the target. The servicer craft begins the simulation at the point located at $x = 100$ m. As the servicer approaches the target, the target rotates. As a result, the electron signal observed by the servicer varies. The number of simulated particles that enter a 0.5 m radius sphere centered at each measurement location is counted, which provides a relative estimate of the particle fluxes that can be expected from the target. To convert this simulated signal from particles to a current in

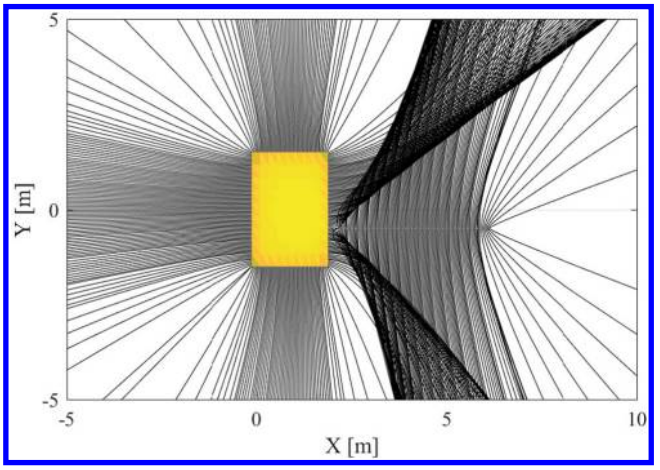

Fig. 11 Close-up view of electrons emitted from target surface. The solar panel is located to the right of the box.

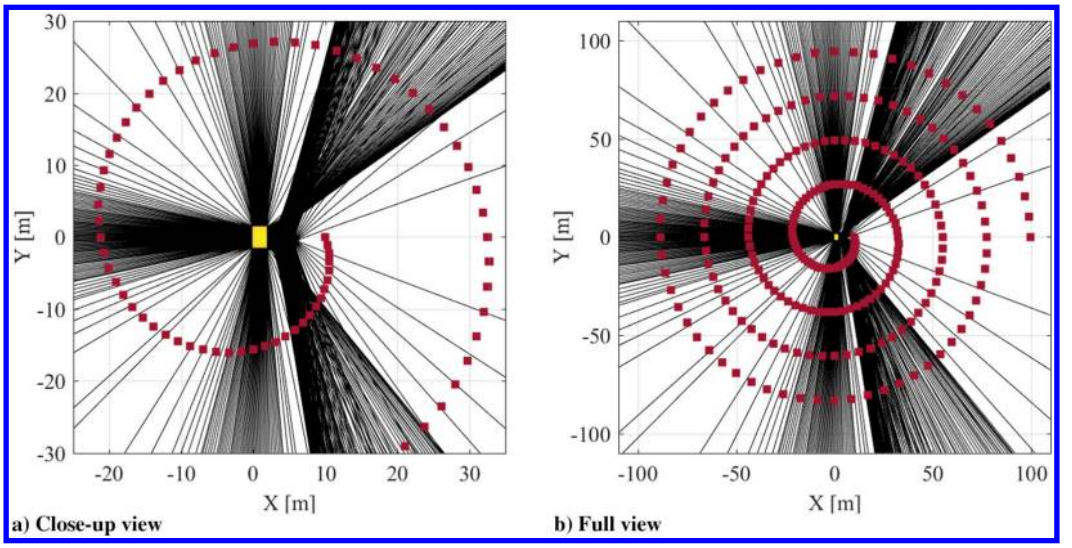

Fig. 12 Views of electrons (black lines) emitted from target surface and servicer craft measurement points (red dots) in the target body frame.

nA, it is assumed that the servicer craft directs a 1 μA beam toward the target and that the beam has a landing energy of 20 keV. While the secondary electron yield (SEY) is often highly material-dependent [47], it can be estimated by the following equation [48]:

$$\delta = \frac{4\delta_{\max}(E_0/E_{\delta\max})}{(1+(E_0/E_{\delta\max}))^2} \tag{4}$$

where δ is the number of secondaries produced for every incident electron (the SEY), E_0 is the landing energy in electron volts, and $\delta_{\max}$ and $E_{\delta\max}$ are the maximum SEY and energy at which the maximum SEY occurs for a given material. The target object is assumed to be aluminum, so values of 0.97 and 300 eV are used for $\delta_{\max}$ and $E_{\delta\max}$, respectively [4]. The first surface for aluminum is actually aluminum oxide under almost all conditions, which increases uncertainty in measuring secondary electron yield; typical values for $\sigma_{\max}$ are around 3 [49]. Given these parameters, the SEY at a landing energy of 20 keV is 0.0565. It is assumed that the 1 μA primary electron beam is expanded to hit the entire target, so the total current emitted from the side of the target hit by the beam is 56.5 nA. To determine which elements are visible from the servicer craft at a given location, the vector normal to the surface of each triangular element is computed. Next, the dot product between the surface normal vectors and the position vector from the target to the servicer is found. Elements for which this dot product are positive are thus visible by the servicer. Though there is a small amount of self-shadowing, it is sufficient for the purposes here to neglect such higher-order effects. Therefore, the number of particles captured at a given measurement point are divided by the particles emitted from the triangular elements visible from the servicer at that point. This fraction is then multiplied by the total 56.5 nA current emitted from the target, scaling the discrete particle simulation to an expected current observed by the servicer at each point.

Figure 13 shows the expected signal measured by the servicing craft as a function of distance from the target. Several interesting features are visible in the data. First, it is apparent that the signal magnitude increases as the servicer gets closer to the target, which is to be expected because the electron current expands out into space as it travels away from the target. However, the focusing effect of the target geometry is more significant that the expansion of the current into space. Electrons do not leave the target isotropically but instead are emitted in specific channels. For example, the peak at 60 m is larger than the peaks from 25 to 50 m. A repetitive pattern is seen in the data, with clear similarities between the peaks at 28, 51, 73, and 96 m; 21, 44, 66, and 88 m; and 13, 37, 60, and 82 m. The repeating pattern is a result of the servicing craft sampling the electron flux from the target as the target rotates multiple times during the approach. There are three "main" peaks in each pattern: the electrons

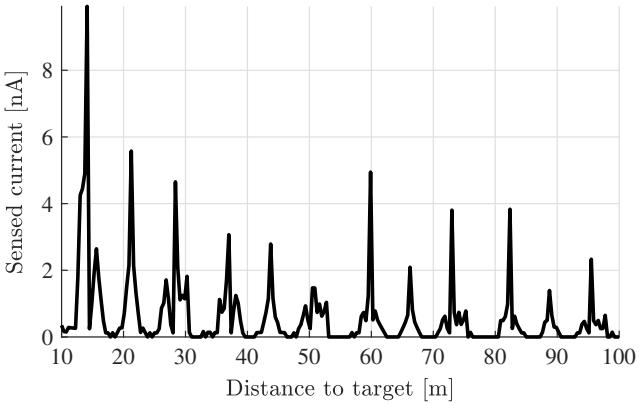

Fig. 13 Sensed secondary electron yield from target, assuming 1 μA beam at 20 keV.

focused by the interior corner where the box and panel are joined, the electrons emitted from the flat side of the box on the opposite of the panel, and then the interior corner on the other side. The target rotates through four full rotations during the simulation, so the pattern of three peaks is observed four times, for a total of 12 main peaks.

The expected signal is useful for determining when the potential of the target is observable. Given the sensitivity of the electron detector on the servicing craft, the simulation results can be used to determine how often the electron signal is large enough for a measurement of the target potential to be obtained. For example, assume a 0.5 nA electron current is required to accurately resolve the potential of the target by measuring the energy of the electron population in the presence of an ambient plasma environment. In this case, a signal greater than 0.5 nA is available for 30% of the sample positions.

Simulations are conducted for target voltages of −500, −1000, and −5000 V. Interestingly, the electron trajectories, and thus the expected signal at the servicer, are independent of the target voltage over the range considered. The relative charge distribution on the target spacecraft is constant regardless of its potential. The total amount of charge on the target scales with voltage, but the relative location of the charge on the target is entirely determined by the geometry of the target. Therefore, the electric field magnitude changes with larger (magnitude) target voltages, but the electric field direction does not change. Because electrons are highly mobile due to their small mass, the electron trajectories are insensitive to surface potential magnitudes, even though the energy of the electron population changes. This is advantageous for the electron-based touchless sensing concept because the signal availability can be computed from the target geometry before the potential of the target is known.

Complex targets, such as the simulated servicing target, have more complicated electric fields than the flat plates used in experiments, which drives significant variations in electron signal availability. The results for one target spacecraft geometry do not readily generalize to others, so such analysis should be carried out for any anticipated target. The following section considers the x-ray signal from the target body.

B. x-Ray Signal Analysis

The methodology applied to simulate bremsstrahlung emission from the environment is derived from the approach in Ref. [50]. Electron fluxes are provided by the mean electron flux IGE-2006 model for geostationary orbit [51]. Electrons in each energy bin are assumed to be monoenergetic with an energy at the average energy of the bin, and Eq. (2) is used to compute the contribution of each population to the bremsstrahlung x-ray spectrum, while Eq. (3) computes the characteristic radiation emission. Higher-level effects, such as solar x-ray secondary fluorescence from the target were considered to be negligible [50].

The passive method relies on the change in total number of photons emitted by hot electrons in the ambient plasma and therefore has no sampling requirement to construct a spectrum. Such a method may be effectively executed with tens or hundreds of photons, which may be collected over several seconds. However, using the assumption of even photon flux from the entire surface of the target body, this method would be sensitive to the apparent area of the target facing the servicer. This apparent projected area is a function of the distance between the spacecraft and also the orientation of the target. Therefore, when comparing the apparent brightness of the target for passive potential estimation, it is important to simultaneously account for target pose and position. The photon flux observed by the servicer as a result of an active electron beam is shown in Fig. 14. Figure 15 illustrates the evolution of the target's apparent brightness due to hot electrons in the ambient plasma. As the target rotates, the projected area seen by the servicer varies by a factor of three, resulting in periodic variation in the sensed flux.

A likely approach to implementing such a technique on orbit would involve comparing expected x-ray fluxes from a target (computed as a function of target attitude, known material properties of the target, and the electron environment measured by the servicer as part of the electron-based sensing method) to the value actually measured over time. The sensed signal would need to be detectable given the x-ray background, which is discussed further in Ref. [50]. Ultimately, this passive technique would require a sophisticated filtering method but could be implemented through an extended Kalman filter (KF) or through other methods.

Experiments demonstrate that detection of ∼1000 photons is sufficient for an accurate bremsstrahlung spectrum and landing energy to be computed. From Fig. 14, this equates to collection periods of tens of seconds at 50 m, but just one second at 10 m. Knowledge of electrostatic potential becomes significantly more important as distance to the target decreases, as electrostatic forces increase with $1/r^2$, and the risk of ESD increases (though ESD risk is minimal at distances greater than a few millimeters). At a distance of

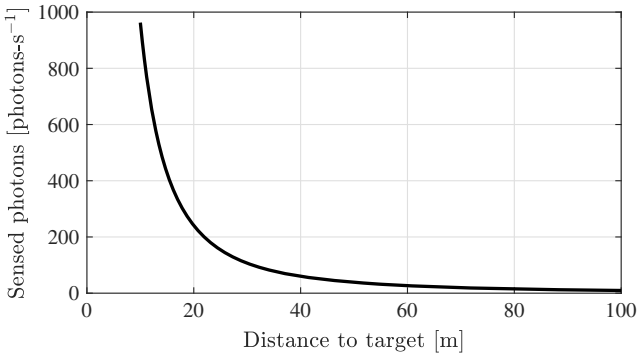

Fig. 14 Photons observed by servicer, with 1 μA, 30 kV electron beam impacting target.

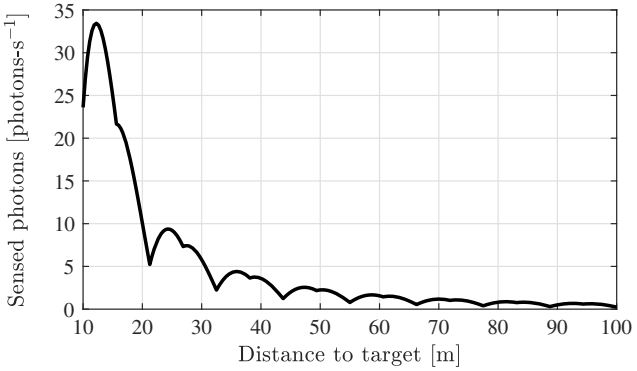

Fig. 15 Photon flux sensed at servicer as a result of target-plasma interactions.

100 m, approximately 10 photons per second are anticipated, while the photon counting rate increases by two orders of magnitude at 10 m. Therefore, the update rate for electrostatic potential estimates can increase from the order of minutes to seconds as the servicer approaches the target.

Several means are available to improve sensed photon yields, which can improve the accuracy of the x-ray spectroscopic potential measurement technique. Increases in detector area could be achieved through the use of x-ray lenses, such as those developed for the neutron star interior composition explorer x-ray telescope aboard the International Space Station, which could increase effective detector area and therefore photon collection rates by up to a factor of 50 [52]. Additionally, the bremsstrahlung yield increases significantly as the landing energy of the electrons increases. Moving from a 20 keV landing energy to 30 keV, for instance, doubles the photon yield. Likewise, increasing beam current would linearly increase photon yields. However, manipulating beam parameters will affect the equilibrium potential of the target body, so such changes must be carefully considered to avoid undesired impacts.

Ultimately, the simulation demonstrates signal availability is analogous to the experimental flat-plate case for both methods. Electron signals are highly dependent on relative geometries but can provide a highly accurate signal when available. The x-ray signal is unaffected by the target orientation when an electron beam is used to generate x rays and shows only moderate dependence on attitude when observing environmentally induced x-ray fluxes. For all cases, signal magnitude increases significantly at short ranges, though the focusing effects of the target geometry can provide strong electron signals at long ranges if relative positions are correctly aligned.

VI. Conclusions

Electron and x-ray spectral methods for remote sensing of spacecraft electrostatic potential have been evaluated through experiments and simulations. A key result is that, if a sufficient signal is available, the electron-based method outperforms the x-ray sensing method, providing accuracies on the order of volts. However, signal availability for this method is limited due to the focusing or diverging of electron trajectories because of electric fields around the target object. This trend is observed experimentally and through simulation of a target spacecraft geometry. In contrast, the x-ray method provides errors two orders of magnitude higher, around 100 V, but signal availability is fairly agnostic to the geometry of the target surface. Further, the x-ray method does not place any requirements on the relative potentials of the two objects, whereas the electron method only works if the electrons are accelerated toward the servicing satellite. Fusing the datasets using an appropriate filter mitigates some of the limitations of each method, thereby producing an estimate of the plate potential with smaller errors and uncertainties that is robust to target orientation. Either electron beams or hot electrons in the ambient plasma can be used for both methods.

Additional avenues for future development include more-sophisticated signal processing techniques to reduce the number of

either electrons or photons required to reconstruct a spectrum or to more accurately compute parameters of interest from the spectra. Continuously conducting spacecraft at a single potential are assumed in this work. However, spacecraft often experience differential charging, in which different parts of the spacecraft charge to different potentials. The effects of differential charging are magnified by nonconducting surface coatings often found on spacecraft, including mylar or kapton. While spacecraft design guidelines recommend maintaining a continuously conducting exterior surface, space environment effects can degrade the efficacy of these coatings. This effect significantly complicates the measurement process for both methods and should be considered in future work. Intermittently pulsing the electron beam would allow the background spectrum in both x rays and electrons to be determined, which may improve the ability to reject such noise sources from measurements. Ultimately, continued research along these lines will advance the remote characterization concept that will be crucial for future on-orbit proximity operations missions.

Acknowledgments

This work was supported through Air Force Office of Scientific Research grant #FA9550-20-1-0025. M. T. Bengtson gratefully acknowledges funding from the National Defense Science and Engineering Graduate Fellowship. The authors would like to acknowledge Dalton Turpen for assistance in building and operating the experimental apparatus.

References

[1] Wilson, K. T. H., and Schaub, H., "Impact of Electrostatic Perturbations on Proximity Operations in High Earth Orbits," *American Astronautical Society/AIAA Astrodynamics Specialist Conference*, ASME Paper 20-657, 2020.

[2] Anderson, P. C., "Characteristics of Spacecraft Charging in Low Earth Orbit," *Journal of Geophysical Research: Space Physics*, Vol. 117, No. A7, 2012. https://doi.org/10.1029/2011JA016875

[3] Mullen, E., Gussenhoven, M., Hardy, D., Aggson, T., Ledley, B., and Whipple, E., "SCATHA Survey of High-Level Spacecraft Charging in Sunlight," *Journal of Geophysical Research: Space Physics*, Vol. 91, No. A2, 1986, pp. 1474–1490. https://doi.org/10.1029/JA091iA02p01474

[4] Lai, S. T., *Fundamentals of Spacecraft Charging: Spacecraft Interactions with Space Plasmas*, Princeton Univ. Press, Princeton, NJ, 2011.

[5] Maxwell, J., and Schaub, H., "Low Earth Orbit Plasma Wake Shaping and Applications to On-Orbit Proximity Operations," *IEEE Transactions on Plasma Science*, Vol. 47, No. 10, 2019, pp. 4760–4769. https://doi.org/10.1109/TPS.2019.2939712

[6] Reed, B. B., Smith, R. C., Naasz, B. J., Pellegrino, J. F., and Bacon, C. E., "The Restore-L Servicing Mission," *AIAA SPACE 2016*, AIAA Paper 2016-5478, 2016.

[7] Sullivan, B., Barnhart, D., Hill, L., Oppenheimer, P., Benedict, B. L., Van Ommering, G., Chappell, L., Ratti, J., and Will, P., "DARPA Phoenix Payload Orbital Delivery System (PODs): 'FedEx to GEO'," *AIAA SPACE 2013 Conference and Exposition*, AIAA Paper 2013-5484, 2013.

[8] Barnhart, D., Sullivan, B., Hunter, R., Bruhn, J., Fowler, E., Hoag, L. M., Chappie, S., Henshaw, G., Kelm, B. E., Kennedy, T., et al., "Phoenix Program Status-2013," *AIAA SPACE 2013 Conference and Exposition*, AIAA Paper 2013-5341, 2013.

[9] Goodman, M., Paez, A., Willis, E., and DeStefano, A., "An Analytic Model for Estimating the First Contact Resistance Needed to Avoid Damaging ESD During Spacecraft Docking in GEO," *Applied Space Environments Conference*, Pasadena, CA, 2019.

[10] Jewison, C., Sternberg, D., McCarthy, B., Miller, D. W., and Saenz-Otero, A., "Definition and Testing of an Architectural Tradespace for On-Orbit Assemblers and Servicers," 2014, https://dspace.mit.edu/handle/1721.1/105518.

[11] Bengtson, M., Wilson, K., Hughes, J., and Schaub, H., "Survey of the Electrostatic Tractor Research for Reorbiting Passive GEO Space Objects," *Astrodynamics*, Vol. 2, No. 4, 2018, pp. 291–305. https://doi.org/10.1007/s42064-018-0030-0

[12] Schaub, H., and Sternovsky, Z., "Active Space Debris Charging for Contactless Electrostatic Disposal Maneuvers," *Advances in Space Research*, Vol. 53, No. 1, 2014, pp. 110–118. https://doi.org/10.1016/j.asr.2013.10.003

[13] Aslanov, V., and Schaub, H., "Detumbling Attitude Control Analysis Considering an Electrostatic Pusher Configuration," *Journal of Guidance, Control, and Dynamics*, Vol. 42, No. 4, 2019, pp. 900–909. https://doi.org/10.2514/1.G003966

[14] Bennett, T., and Schaub, H., "Touchless Electrostatic Three-Dimensional Detumbling of Large Axi-Symmetric Debris," *Journal of the Astronautical Sciences*, Vol. 62, No. 3, 2015, pp. 233–253. https://doi.org/10.1007/s40295-015-0075-8

[15] Karavaev, Y. S., Kopyatkevich, R. M., Mishina, M. N., Mishin, G. S., Papushev, P. G., and Shaburov, P. N., "The Dynamic Properties of Rotation and Optical Characteristics of Space Debris at Geostationary Orbit," *Advances in the Astronautical Sciences*, Vol. 119, 2004.

[16] Stevenson, D., and Schaub, H., "Multi-Sphere Method for Modeling Electrostatic Forces and Torques," *Advances in Space Research*, Vol. 51, No. 1, 2013, pp. 10–20. https://doi.org/10.1016/j.asr.2012.08.014

[17] Bengtson, M., Hughes, J., and Schaub, H., "Prospects and Challenges for Touchless Sensing of Spacecraft Electrostatic Potential Using Electrons," *IEEE Transactions on Plasma Science*, Vol. 47, No. 8, 2019.

[18] Bengtson, M., Wilson, K., and Schaub, H., "Simulations and Experimental Results of Electron Method for Remote Spacecraft Charge Sensing," *Applied Space Environments Conference*, Pasadena, CA, 2019.

[19] Wilson, K., and Schaub, H., "X-Ray Spectroscopy for Electrostatic Potential and Material Determination of Space Objects," *IEEE Transactions on Plasma Science*, Vol. 47, No. 8, 2019.

[20] Wilson, K., and Schaub, H., "Electron-Induced X-Rays for Remote Potential Sensing," *Applied Space Environments Conference*, Pasadena, CA, 2019.

[21] Chung, M., and Everhart, T., "Simple Calculation of Energy Distribution of Low-Energy Secondary Electrons Emitted from Metals Under Electron Bombardment," *Journal of Applied Physics*, Vol. 45, No. 2, 1974, pp. 707–709. https://doi.org/10.1063/1.1663306

[22] Bruining, H., *Physics and Applications of Secondary Electron Emission*, Pergamon Press, London, 1954, https://www.amptek.com/-/media/ametekamptek/documents/products/specs/x123-specs.pdf [retrieved 10 April 2022].

[23] Knudsen, W. C., Spenner, K., Bakke, J., and Novak, V., "Pioneer Venus Orbiter Planar Retarding Potential Analyzer Plasma Experiment," *IEEE Transactions on Geoscience and Remote Sensing*, Vol. GE-18, 1980, pp. 54–59, https://ieeexplore.ieee.org/document/8273755 [retrieved 10 April 2022]. https://doi.org/10.1109/TGRS.1980.350261

[24] Case, A. W., Kasper, J. C., Stevens, M. L., Korreck, K. E., Paulson, K., Daigneau, P., Caldwell, D., Freeman, M., Henry, T., Klingensmith, B., et al., "The Solar Probe Cup on the Parker Solar Probe," *Astrophysical Journal Supplement Series*, Vol. 246, No. 2, 2020, p. 43. https://doi.org/10.3847/1538-4365/ab5a7b

[25] Pollock, C., Moore, T., Jacques, A., Burch, J., Gliese, U., Saito, Y., Omoto, T., Avanov, L., Barrie, A., Coffey, V., et al., "Fast Plasma Investigation for Magnetospheric Multiscale," *Space Science Reviews*, Vol. 199, Nos. 1–4, 2016, pp. 331–406. https://doi.org/10.1007/s11214-016-0245-4

[26] Whittlesey, P. L., Larson, D. E., Kasper, J. C., Halekas, J., Abatcha, M., Abiad, R., Berthomier, M., Case, A., Chen, J., Curtis, D. W., et al., "The Solar Probe Analyzers—Electrons on the Parker Solar Probe," *Astrophysical Journal Supplement Series*, Vol. 246, No. 2, 2020, p. 74. https://doi.org/10.3847/1538-4365/ab7370

[27] Enloe, C., "High-Resolution Retarding Potential Analyzer," *Review of Scientific Instruments*, Vol. 65, No. 2, 1994, pp. 507–508. https://doi.org/10.1063/1.1145167

[28] Robertson, S., Sternovsky, Z., and Walch, B., "Reduction of Asymmetry Transport in the Annular Penning Trap," *Physics of Plasmas*, Vol. 11, No. 5, 2004, pp. 1753–1756. https://doi.org/10.1063/1.1688337

[29] Duane, W., and Hunt, F., "On X-Ray Wave-Lengths," *Physical Review*, Vol. 6, No. 2, 1915, pp. 166–172. https://doi.org/10.1103/PhysRev.6.166

[30] Lamoureux, M., and Charles, P., "General Deconvolution of Thin-Target and Thick-Target Bremsstrahlung Spectra to Determine Electron Energy Distributions," *Radiation Physics and Chemistry*, Vol. 75, No. 10, 2006. https://doi.org/10.1016/j.radphyschem.2006.06.006

[31] "X-123 Si-PIN x-Ray Detector," Amptek, Inc. TR, 2018.

[32] Castellano, G., Osán, J., and Trincavelli, J., "Analytical Model for the Bremsstrahlung Spectrum in the 0.25–20 keV Photon Energy Range," *Spectrochimica Acta Part B: Atomic Spectroscopy*, Vol. 59, No. 3, 2004, pp. 313–319.
https://doi.org/10.1016/j.sab.2003.11.008

[33] McCall, G. H., "Calculation of X-Ray Bremsstrahlung and Characteristic Line Emission Produced by a Maxwellian Electron Distribution," *Journal of Physics D: Applied Physics*, Vol. 15, No. 5, 1982, pp. 823–831.
https://doi.org/10.1088/0022-3727/15/5/012

[34] Bengtson, M., Wilson, K. T. H., and Schaub, H., "Broad-Spectrum Electron Gun for Laboratory Simulation of Orbital Environments," *AIAA SciTech Conference*, 2021.

[35] Bengtson, M., and Schaub, H., "Remote Sensing of Spacecraft Potential at Geosynchronous Orbit Using Secondary and Photo Electrons," *AIAA Scitech 2019 Forum*, AIAA Paper 2019-0311, 2019.

[36] Wilson, K. T. H., Bengtson, M., Maxwell, J., Alvaro Romero Calvo, Á., and Schaub, H., "Characterization of the ECLIPS Space Environments Simulation Facility," *AIAA SciTech Conference*, 2021.

[37] Moore, C. S., Caspi, A., Woods, T. N., Chamberlin, P. C., Dennis, B. R., Jones, A. R., Mason, J. P., Schwartz, R. A., and Tolbert, A. K., "The Instruments and Capabilities of the Miniature X-Ray Solar Spectrometer (MinXSS) CubeSats," *Solar Physics*, Vol. 293, No. 2, 2018, pp. 1–40.
https://doi.org/10.1007/s11207-018-1243-3

[38] Fanelli, L., Noel, S., Earle, G. D., Fish, C., Davidson, R. L., Robertson, R. V., Marquis, P., Garg, V., Somasundaram, N., Kordella, L., and Kennedy, P., "A Versatile Retarding Potential Analyzer for Nano-Satellite Platforms," *Review of Scientific Instruments*, Vol. 86, No. 12, 2015, Paper 124501.
https://doi.org/10.1063/1.4937622

[39] Wilson, K., Bengtson, M., and Schaub, H., "X-ray Spectroscopic Determination of Electrostatic Potential and Material Composition for Spacecraft: Experimental Results," *Space Weather*, Vol. 18, No. 4, 2020, pp. 1–10.
https://doi.org/10.1029/2019SW002342

[40] Alvaro Romero Calvo, Á., Schaub, H., and Cano Gómez, G., "Electron Beam Expansion and Deflection Uncertainty for Active Spacecraft Charging Applications," *AIAA SciTech Conference*, 2021.

[41] Mazur, J. E., Fennell, J. F., Roeder, J. L., O'Brien, P. T., Guild, T. B., and Likar, J. J., "The Timescale of Surface-Charging Events," *IEEE Transactions on Plasma Science*, Vol. 40, No. 2, 2012, pp. 237–245.
https://doi.org/10.1109/TPS.2011.2174656

[42] Akhlaghi, S., Zhou, N., and Huang, Z., "Adaptive Adjustment of Noise Covariance in Kalman Filter for Dynamic State Estimation," CoRR, Vol. abs/1702.00884, 2017, http://arxiv.org/abs/1702.00884 [retrieved 10 April 2022].

[43] Harrington, R. F., *Field Computation by Moment Methods*, Wiley-Institute of Electrical and Electronics Engineers Press, Piscataway, NJ, 1993.

[44] Chakrabarty, S., and Jyoti, R., "Absolute Charging Analysis of Space-Craft Bodies Using Method of Moments (MoM)," *2015 Institute of Electrical Aand Electronics Engineers Applied Electromagnetics Conference (AEMC)*, Inst. of Electrical and Electronics Engineers, New York, 2015, pp. 1–2.

[45] Boris, J. P., "Relativistic Plasma Simulation-Optimization of a Hybrid Code," *Proceedings of Fourth Conference on the Numerical Simulations of Plasmas*, Naval Research Lab., Washington, D.C., 1970, pp. 3–67.

[46] Qin, H., Zhang, S., Xiao, J., Liu, J., Sun, Y., and Tang, W. M., "Why Is Boris Algorithm so Good?" *Physics of Plasmas*, Vol. 20, No. 8, 2013, Paper 084503.
https://doi.org/10.1063/1.4818428

[47] Lundgreen, P., and Dennison, J., "Strategies for Determining Electron Yield Material Parameters for Spacecraft Charge Modeling," *Space Weather*, Vol. 18, No. 4, 2020.
https://doi.org/10.1029/2019SW002346

[48] Draine, B., and Salpeter, E., "On the Physics of DUST Grains in Hot Gas," *Astrophysical Journal*, Vol. 231, 1979, pp. 77–94.
https://doi.org/10.1086/157165

[49] Hoffmann, R., Dennison, J. R., Thomson, C. D., and Albretsen, J., "Low-Fluence Electron Yields of Highly Insulating Materials," *IEEE Transactions on Plasma Science*, Vol. 36, No. 5, 2008, pp. 2238–2245.
https://doi.org/10.1109/TPS.2008.2004226

[50] Wilson, K. T. H., and Schaub, H., "Environmental x-Ray Considerations for Bremsstrahlung-Based Surface Potential Determination," *AIAA SciTech*, 2020.

[51] Sicard-Piet, A., Bourdarie, S., Boscher, D., Friedel, R. H. W., Thomsen, M., Goka, T., Matsumoto, H., and Koshiishi, H., "A New International Geostationary Electron Model: IGE-2006, from 1 keV to 5.2 MeV," *Space Weather*, Vol. 6, No. 7, 2008.
https://doi.org/10.1029/2007SW000368

[52] Okajima, T., Soong, Y., Balsamo, E. R., Enoto, T., Olsen, L., Koenecke, R., Lozipone, L., Kearney, J., Fitzsimmons, S., Numata, A., Kenyon, S. J., Arzoumanian, Z., and Gendreau, K., "Performance of NICER Flight x-Ray Concentrator," *Space Telescopes and Instrumentation 2016: Ultraviolet to Gamma Ray*, Vol. 9905, edited by J.-W. A. den Herder, T. Takahashi, and M. Bautz, International Soc. for Optics and Photonics, Soc. of Photo-Optical Instrumentation Engineers, Bellingham, WA, 2016, pp. 1495–1501.
https://doi.org/10.1117/12.2234436

V. J. Lappas
Associate Editor